Soil Dynamics and Earthquake Engineering 148 (2021) 106723

Contents lists available at ScienceDirect

Soil Dynamics and Earthquake Engineering

journal homepage: www.elsevier.com/locate/soildyn

Dominant responses of bridge abutments

Davide Noè Gorini [a,*], Luigi Callisto [a], Andrew J. Whittle [b]

[a] Sapienza University of Rome, Italy
[b] Massachusetts Institute of Technology, Cambridge, MA, USA

ARTICLE INFO

Keywords:
Bridge abutments
Inertial effects
Nonlinear behaviour
OpenSees

ABSTRACT

Under seismic conditions a bridge abutment can transfer significant inertial effects to the superstructure due to its interaction with a large volume of soil. These effects can lead to a marked dynamic amplification of the abutment response that should be accounted for in bridge design. In order to quantify these effects, we present analytical solutions for the modal characteristics of the soil-abutment system at small strains, expressed in terms of the vibration periods and mass participation factors for the approach embankment considering different directions of motion. The effect of nonlinear soil behaviour is also investigated through nonlinear numerical analyses of the soil-abutment system in OpenSees, which establish the dependence of the vibration periods on the intensity of the external perturbation. The numerical results were used as a benchmark to validate the analytical predictions at small strains; they can also provide some indication on the applicability of the analytical formulation at medium and large strain levels. The proposed method of dynamic identification can be used as a tool to evaluate the dynamic characteristics of bridge abutments, which can be in turn regarded as the inertial features of macroelement representations for abutments in the structural analysis of bridges.

1. Introduction

It is well established that the dynamic characteristics of bridges can be significantly affected by interactions between the abutment and approach embankment fills, resulting in excessive deformation demands on substructural elements (Mackie and Stojadinovic 2003, Kappos et al., 2007 [1,2]). These effects are especially significant in the case of integral bridge abutments, as highlighted in a recent review by Mitoulis (2020) [3]. This has been observed from the measured seismic performance of two instrumented highway bridges in California (Painter Street at US101, Goel and Chopra 1997; Meloland Road at I-8, Werner et al., 1978, Wilson and Tan 1990a [4–6]). For these medium-span bridges soil deformations are concentrated within a volume of the approach embankment that interacts dynamically with the abutments, causing substantial alteration of the system's dynamic characteristics. Strong motion events can engage the nonlinear behaviour of the system and cause irreversible displacements of the abutment with consequent permanent internal forces in the superstructure. In these conditions, the ultimate capacity of the soil-abutment system can be attained momentarily during the event, when longitudinal inertial forces transferred by the deck mobilize the passive resistance of the soil (Shamsabadi et al., 2005, Shamsabadi et al., 2007 [7,8]) or through more complex failure mechanisms generated by multi-axial loading (Gorini et al., 2020a [9]). Several numerical studies have also shown the importance of inertial effects developing in the approach embankments on the seismic performance of girder bridges (Kotsoglou and Pantazopoulou 2007, 2009a, Elgamal et al., 2008, Taskari and Sextos 2015, Gorini and Callisto 2020, Gorini et al., 2020b [10–15]). The performance of the entire bridge is then the result of the combination of the inertial effects developing in the soil-abutment system and in the superstructure (piers and deck). These effects are characterised by a phase difference caused by the disparate dynamic response of the abutment and superstructure and by the spatial variability of the ground motion, which is particularly significant for medium- to long-span, tall bridges (Mylonakis et al., 1999, Sextos et al., 2003, Lam et al., 2004 [16–18]).

From a practical perspective, bridge design typically involves analyses at different levels of complexity and detail. In preliminary seismic design soil-structure interactions are often considered using a substructure approach (Kramer 1996 [19]) wherein the performance of a bridge is evaluated through a response spectrum modal analysis using a global structural model, whose dynamic perturbation comes from an independent evaluation of site response effects. The soil-structure interactions are simulated through linear spring-dashpot elements that either have frequency-dependent features, or are combined with

* Corresponding author. Dept. of Structural and Geotechnical Engineering, via Eudossiana 18, 00184, Roma, Italy.
E-mail address: davideno.gorini@uniroma1.it (D. Noè Gorini).

https://doi.org/10.1016/j.soildyn.2021.106723
Received 5 September 2020; Received in revised form 9 March 2021; Accepted 10 March 2021
Available online 6 June 2021

participating masses to reproduce the inertial effects associated with the multi-modal response of the embankment (Zhang and Makris 2002 [20], Kotsoglou and Pantazopoulou 2007, 2009a, b [10,11,21]; Mitoulis 2017 [22], Stefanidou et al., 2017 [23]). The subsequent design verification stage may involve dynamic, nonlinear time-domain analysis of the global structural model. These models can include more complex representation of the frequency-dependent embankment-abutment interactions, that evolve with the motion amplitude through a macroelement approach (e.g., Roscoe and Schofield 1956, Nova and Montrasio 1991, Cremer et al., 2002 [24–26]). For example, Gorini et al. (2020a) [15] developed a plasticity-based, inertial macroelement to represent soil-abutment interaction through the introduction of participating masses.

Within all these approaches, the dynamic characterisation of bridge embankments is still an open question, to which several studies were devoted over the last years. Wilson and Tan (1990a, 1990b) [6,27] presented an analytical model for the estimation of the seismic response of highway overpasses considering the interaction of the abutments with the earth embankments. Using the shear beam concept and assuming linear elastic soil behaviour, they determined the transverse stiffness of the approach embankment subjected to loads applied to the top of the embankment, assuming an effective length of fill equal to the length of the wing walls. Wissawapaisal (1999) [28] proposed an interpretive model to evaluate the dynamic effects of abutments in the longitudinal direction of the bridge, in which the embankment is represented by an assembly of lumped masses connected through nonlinear shear springs to the abutment. While both of these models assume an effective length of the embankment that participates to the dynamic response of the bridge, they neglect the contribution of the foundation soil. More recently, Kotsoglou and Pantazopoulou (2007) [10] used an analytical approach to provide solutions for the modal characteristics of the embankments in the transverse direction assuming linear soil behaviour but neglecting the compliance of the foundation soil.

Taking the procedure proposed in Ref. [10] as a starting point, the current paper develops analytical solutions for the modal characteristics of the soil-abutment system at small strains along different directions of motion. We propose a straightforward calibration procedure of the input quantities that is able to account for the contribution of the foundation soil. The analytical solutions are then compared with the results of finite element dynamic analyses for a reference case study. These dynamic simulations enable us to investigate the effects of nonlinear behaviour of soil on the dominant responses of the reference abutment.

2. An analytical method for the dynamic identification of bridge approach embankments

This section describes an analytical method to evaluate the modal characteristics of bridge embankments at small strain levels along different directions of motion. We generalize the solutions proposed in Ref. [10] for multi-component seismic excitation. Fig. 1 shows the geometry of the embankment used in this study. We assume an equivalent rectangular cross section for the embankment (width B and height H).

2.1. Equations of motion

Consider the motion of an embankment along the coordinate directions of the deck-abutment contact $\{x,y,z\}$ (Fig. 1) induced by the seismic excitation. As a simplifying hypothesis, the displacement field u_i was assumed uniform in the transverse direction, i.e. the embankment width was taken to be significantly smaller than the shortest wavelengths of interest. Hence, such that: $u_i(x,y,z,t) = u_i(y,z,t) = u_x(y,z,t)\cdot e_x + u_y(y,z,t)\cdot e_y + u_z(y,z,t)\cdot e_z$ (where e_i is the basis vector). The equations of motion describing the dynamic response of bridge embankments along different directions were derived considering an infinitesimal segment of the embankment of width B, height dz and depth dy. Fig. 1b,c,d show the stresses acting on the infinitesimal volume dV, where $S_{ij}(y,z,t)$ (i = x,

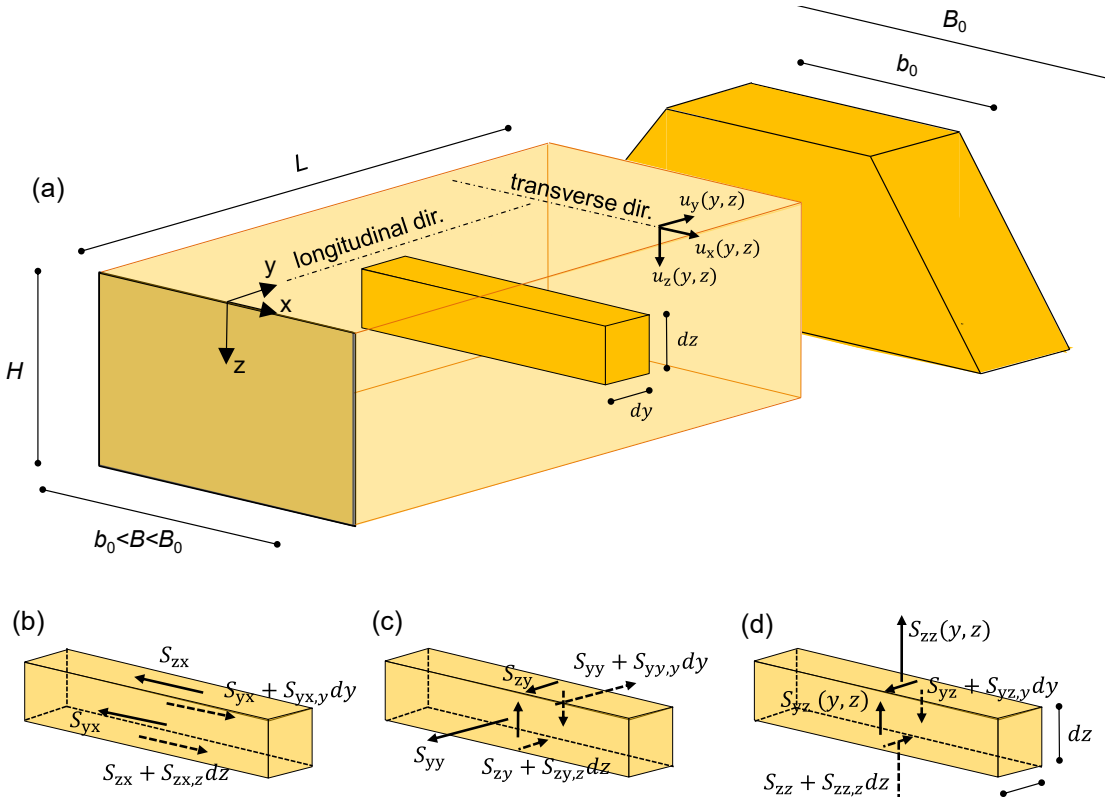

Fig. 1. (a) Model of the embankment for the analytical method; forces acting on an infinitesimal soil segment in the (b) transverse, (c) longitudinal and (d) vertical direction.

y,*z*) represents the shear stress in the *j*-direction acting on a surface of normal *i*. Also, the infinitesimal soil volume is subjected to body forces $F_i(y,z)$ (i = *x*,*y*,*z*) directed as the positive directions of the coordinate axes *x*, *y* and *z*. The transverse motion of the embankment induces only shear strains because $u_i(y,z,t)$ does not vary across the embankment. The motion in the other directions provokes instead a combined volumetric-shear deformation: a shear deformation due to the shear stresses $S_{ij}(y,z,t)$ (i≠j) and a volumetric deformation induced by the difference between the normal stresses $S_{ii}(y,z,t)$ and $S_{ii}(y+\Delta y,z+\Delta z,t)$. This condition can be deemed representative of the embankment response to a combination of shear and compressional waves, propagating in the longitudinal and vertical directions.

Under the above assumptions, the local force equilibrium equations read:

$$F_x(y,z,t) + S_{zx,z}(y,z,t) + S_{yx,y}(y,z,t) = 0 \tag{1}$$

$$F_y(y,z,t) + S_{zy,z}(y,z,t) + S_{yy,y}(y,z,t) = 0 \tag{2}$$

$$F_z(y,z,t) + S_{yz,y}(y,z,t) + S_{zz,z}(y,z,t) = 0 \tag{3}$$

in which an indicial notation is used to denote derivatives, i.e. $u_{i,j}(y,z,t)$ stands for the derivative of the displacement component $u_i(y,z,t)$ with respect to the variable *j*. Note that, because of the assumption of the stress and displacement fields, the derivative with respect to *x* does not appear in the above equations.

To deal with analytically manageable equations of motion, the soil is regarded as a homogenous, linearly elastic and isotropic medium, that in addition shows an uncoupled response along different directions. The former assumption relates to the small strain behaviour of soil, while the validity of the latter was verified a posteriori through the finite element dynamic simulations described in Section 3.1. Hence the displacement field of the embankment can be regarded as three independent, uni-axial deformation modes along the coordinate directions *x*, *y* and *z*. In this manner, the shear stresses can be simply written as:

$$S_{ij}(y,z,t) = G \cdot u_{j,i} \tag{4}$$

in which *G* is the shear modulus of soil; the normal stresses can be instead assumed as a function of a constant oedometer modulus E_{oed} as follows:

$$S_{ii}(y,z,t) = E_{oed} \cdot u_{i,i} \; i = y,z. \tag{5}$$

Under dynamic conditions, the term $F_i(y,z,t)$ can be regarded as an inertial body force and therefore can be written as $F_i(y,z,t) = -\rho_s \cdot u_{i,tt}(y,z,t)$, assuming a constant soil density ρ_s. Substituting Eqs. (4) and (5) into Eqs. (1)–(3), the equations of motion for a combined volumetric-shear mode assume the following form:

$$u_{x,tt}(y,z,t) - V_s^2 \cdot \left[u_{x,yy}(y,z,t) + u_{x,zz}(y,z,t)\right] = 0 \tag{6}$$

$$u_{y,tt}(y,z,t) - V_p^2 \cdot u_{y,yy}(y,z,t) - V_s^2 \cdot u_{y,zz}(y,z,t) = 0 \tag{7}$$

$$u_{z,tt}(y,z,t) - V_s^2 \cdot u_{z,yy}(y,z,t) - V_p^2 \cdot u_{z,zz}(y,z,t) = 0 \tag{8}$$

where $V_s = \sqrt{G/\rho_s}$ and $V_p = \sqrt{E_{oed}/\rho_s}$ are the shear and compressional wave velocity of soil, respectively. Eqs. (6)–(8) can be solved in closed form by using separation of variables once the boundary and initial conditions are set.

Consider the case of an embankment perturbed by a displacement field applied to the front wall of the abutment, representing the motion induced by the seismic actions transferred to the abutment by the deck. In this condition, the base of the embankment can be reasonably assumed as fixed while at the top the shear strain are equal to zero: $u_{i,z}(y, z = 0,t) = 0$. In the longitudinal direction, instead, we consider a free embankment motion (no strains) at the abutment wall and a fixed boundary at the distal end, where the embankment is no longer interacting with the abutment: $u_{i,y}(y = 0,z,t) = 0$ and $u_i(y = L,z,t) = 0$, respectively.

The reader can refer to Ref. [10] for the application of the method in the transverse direction of motion (Eq. (6)) while the derivation of the solution in the other directions (Eqs. (7) and (8)) is reported in Appendix A. The resulting displacement field assumes the following form:

$$u_i(y,z,t) = A \cdot C \cdot \cos\left(z \cdot \sqrt{-\mu_z}\right) \cdot \cos\left(y \cdot \sqrt{-\lambda}\right) \cdot \cdot \left[E \cdot \cos\left(t \cdot \omega_{i,n}\right) + F \cdot \sin\left(t \cdot \omega_{i,n}\right)\right], \; i = x,y,z. \tag{9}$$

in which *A*, *C*, *E* and *F* are integration constants, $\omega_{i,n}$ is the circular frequency associated with the *n*th mode in the *i*-direction, while μ_z and λ are parameters of the problem, given by Eqs. (36) and (43) (Appendix A): they represent modal shape ratios of the embankment that depend on the embankment geometry and vary with the order *n* of the vibration mode.

2.2. Modal characteristics

In the following we analyse free vibrations in order to study the modal characteristics of bridge approach embankments. The dynamic characteristics of the embankment were evaluated through the following definition of the natural shapes of vibration:

$$\Phi_i(y,z) = \frac{u_i(y,z,t)}{u_{i,0}(0,0,t)} = \cos\left(z \cdot \sqrt{-\mu_z}\right) \cdot \cos\left(y \cdot \sqrt{-\lambda}\right), \; i = x,y,z \tag{10}$$

where $u_{i,0}(0,0,t) = A \cdot C$ is the generalised coordinate (point of reference). The modal functions $\Phi_i(y,z)$ represent the part of the overall solution, Eq. (9), that depend only on the space variables *y* and *z*: they describe the modal shapes of the embankment in the three coordinate directions, neglecting the interaction between different degrees of freedom by hypothesis. Fig. 2 depicts the resulting first and second modal shapes of the reference embankment for each direction of motion. It appears evident that the modal function $\Phi_i(y,z)$ represents a normalised, harmonic distribution of the displacements in the *i*-direction, with zero displacement in correspondence of the base of the embankment and at the effective distance from the abutment wall in the longitudinal direction, as prescribed by the boundary conditions. The different deformation modes that characterise the motion along different directions lead to a variable participation of the soil mass to the dynamic response, aspect that is demonstrated through the following development.

Since the modal shape $\Phi_i(y,z)$ is not a function of time, the displacement in the *i*-direction can be written as $u_i(y,z,t) = \Phi_i(y,z) \times T_i(t)$, where $T_i(t)$ is the part of the solution depending on time only. If Eq. (10) is substituted into the equations of motion, Eqs. (6)–(8), one obtains:

$$\Phi_x(y,z) \cdot T_{x,tt}(t) - V_s \cdot \left[\Phi_{x,yy}(y,z) \cdot T_x(t) + \Phi_{x,zz}(y,z) \cdot T_x(t)\right] = 0 \tag{11}$$

$$\Phi_y(y,z) \cdot T_{y,tt}(t) - V_p^2 \cdot \Phi_{y,yy}(y,z) \cdot T_y(t) - V_s^2 \cdot \Phi_{y,zz}(y,z) \cdot T_y(t) = 0 \tag{12}$$

$$\Phi_z(y,z) \cdot T_{z,tt}(t) - V_s^2 \cdot \Phi_{z,yy}(y,z) \cdot T_z(t) - V_p^2 \cdot \Phi_{z,zz}(y,z) \cdot T_z(t) = 0. \tag{13}$$

The principle of virtual work can be applied to derive the global equations of motion, determining the virtual work produced by the forces acting on the system when undergoing a virtual displacement $\Phi_i(y,z)$ consistent with the boundary conditions. In this way, Eqs. (11)–(13) can be rewritten in the following canonical form:

$$M_{i,n} \cdot T_{i,tt}(t) - K_{i,n} \cdot T_i(t) = 0, \; i = x,y,z \tag{14}$$

that contains explicitly the modal mass $M_{i,n}$ and the modal stiffness $K_{i,n}$ of the embankment for each direction of motion *i* and mode *n*. Note that also the time-dependent function T_i depends on the mode considered through the respective circular frequency $\omega_{i,n}$ (see Appendix A). Hence Eq. (14) represents, for each direction, the equation of motion corresponding to the *n*th vibration mode. As a consequence of the directional

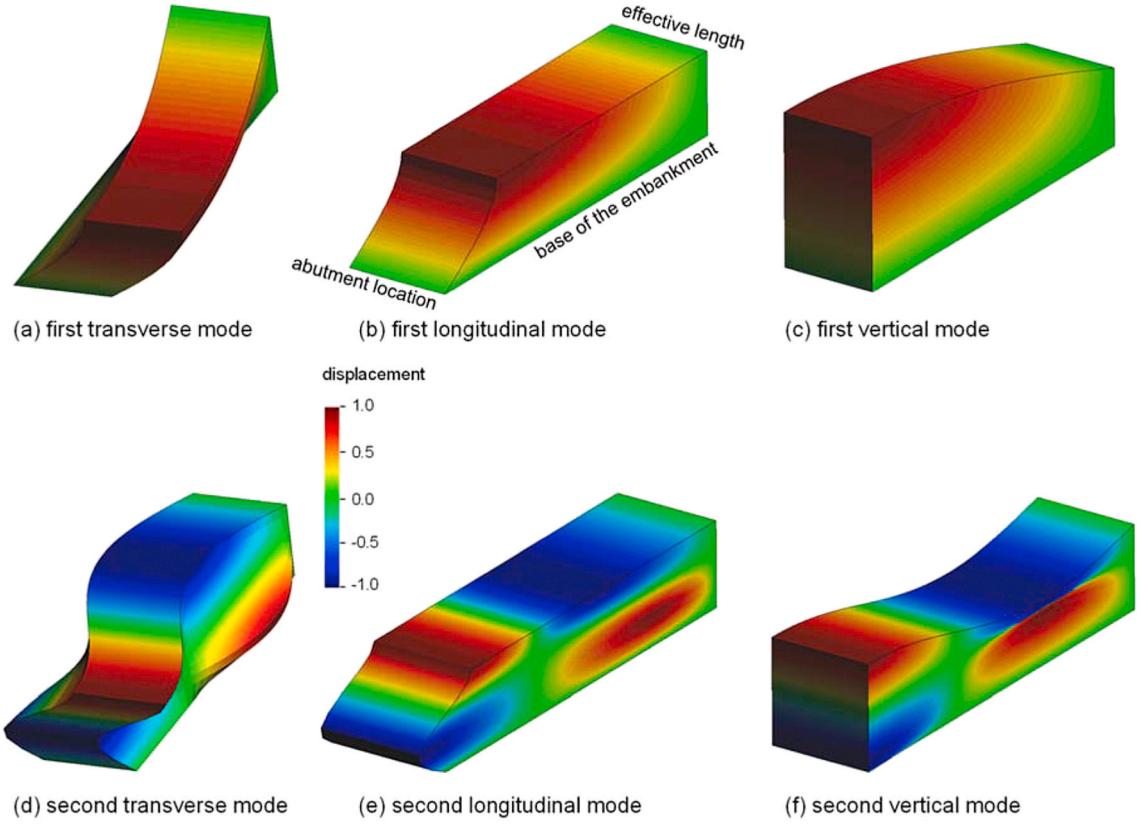

Fig. 2. First (a,b,c) and second (d,e,f) modal shapes of the embankment obtained with the analytical solutions (contour fill of the displacement field: blue = -1, green = 0, red = 1).

uncoupling of the soil response, it was proved that these modal equations are independent on each other, since the modes satisfy the orthogonality conditions (Clough and Penzien 2003 [29]). The analytical details of this check are omitted for conciseness.

The modal masses are given by the following expression:

$$M_{i,n} = B \cdot \rho_s \cdot \int_0^L \int_0^H \Phi_i(y,z)^2 \cdot dz \cdot dy, \; i = x,y,z; \; n \in N_0^+ \tag{15}$$

representing the mass of the effective volume of soil $V = B{\cdot}L{\cdot}H$ participating to the dynamic response of the embankment multiplied locally by the modal shape $\Phi_i(y,z)$. The expressions for the modal stiffness are:

$$K_{x,n} = B \cdot G \cdot \left(\int_0^L \int_0^H \Phi_x(y,z) \cdot \Phi_{x,zz}(y,z) \cdot dz \cdot dy + \right. \\ \left. + \int_0^L \int_0^H \Phi_x(y,z) \cdot \Phi_{x,yy}(y,z) \cdot dz \cdot dy, \; n \in N_0^+ \right) \tag{16}$$

$$K_{y,n} = B \cdot E_{oed} \cdot \int_0^L \int_0^H \Phi_y(y,z) \cdot \Phi_{y,yy}(y,z) \cdot dz \cdot dy \\ + B \cdot G \cdot \int_0^L \int_0^H \Phi_y(y,z) \cdot \Phi_{y,zz}(y,z) \cdot dz \cdot dy, \; n \in N_0^+ \tag{17}$$

$$K_{z,n} = B \cdot G \cdot \int_0^L \int_0^H \Phi_z(y,z) \cdot \Phi_{z,yy}(y,z) \cdot dz \cdot dy \\ + B \cdot E_{oed} \cdot \int_0^L \int_0^H \Phi_z(y,z) \cdot \Phi_{z,zz}(y,z) \cdot dz \cdot dy, \; n \in N_0^+ \tag{18}$$

which differ for the directions of motion considered because they include the effects associated with the different deformation mechanisms induced by the horizontal and vertical ground motion. For a parallelepiped-shaped embankment, Eqs. (15)–(18) can be integrated by parts and the relative closed-form solutions are reported below:

$$M_{i,n} = \frac{B \cdot \rho_s}{2 \cdot \sqrt{\lambda \cdot \mu_z}} \cdot f_h(L,n) \cdot f_v(H,n), \; n \in N_0^+ \tag{19}$$

$$K_{x,n} = -\frac{B \cdot G \cdot (\lambda + \mu_z)}{2 \cdot \sqrt{\lambda \cdot \mu_z}} \cdot f_h(L,n) \cdot f_v(H,n), \; n \in N_0^+ \tag{20}$$

$$K_{y,n} = -\frac{B \cdot (E_{oed} \cdot \lambda + G \cdot \mu_z)}{2 \cdot \sqrt{\lambda \cdot \mu_z}} \cdot f_h(L,n) \cdot f_v(H,n), \; n \in N_0^+ \tag{21}$$

$$K_{z,n} = -\frac{B \cdot (G \cdot \lambda + E_{oed} \cdot \mu_z)}{2 \cdot \sqrt{\lambda \cdot \mu_z}} \cdot f_h(L,n) \cdot f_v(H,n), \; n \in N_0^+ \tag{22}$$

in which the two functions f_h and f_v model the modal shapes in the horizontal and vertical directions, respectively, depending only on the embankment geometry and the order of the mode considered:

$$f_h(L,n) = \left[L \cdot \sqrt{-\lambda} + \sin\left(L \cdot \sqrt{-\lambda} \right) \cdot \cos\left(L \cdot \sqrt{-\lambda} \right) \right], \; n \in N_0^+ \tag{23}$$

$$f_v(H,n)=\left[H\cdot\sqrt{-\mu_z}+\sin\left(H\cdot\sqrt{-\mu_z}\right)\cdot\cos\left(H\cdot\sqrt{-\mu_z}\right)\right],\ n\in N_0{}^+. \quad (24)$$

As a result, the *n*th circular frequencies of the embankment can be computed as below:

$$\omega_{x,n}=\sqrt{\frac{K_{x,n}}{M_{x,n}}}=\frac{\pi\cdot V_s}{2}\cdot\sqrt{\lambda+\mu_z}=\frac{\pi\cdot V_s\cdot(1+2\cdot n)}{2}\cdot\sqrt{\frac{1}{L^2}+\frac{1}{H^2}},\ n\in N_0{}^+ \quad (25)$$

$$\omega_{y,n}=\frac{\pi}{2}\cdot\sqrt{V_p{}^2\cdot\lambda+V_s{}^2\cdot\mu_z}=\frac{\pi\cdot(1+2\cdot n)}{2}\cdot\sqrt{\frac{V_p{}^2}{L^2}+\frac{V_s{}^2}{H^2}},\ n\in N_0{}^+ \quad (26)$$

$$\omega_{z,n}=\frac{\pi}{2}\cdot\sqrt{V_s{}^2\cdot\lambda+V_p{}^2\cdot\mu_z}=\frac{\pi\cdot(1+2\cdot n)}{2}\cdot\sqrt{\frac{V_s{}^2}{L^2}+\frac{V_p{}^2}{H^2}},\ n\in N_0{}^+ \quad (27)$$

showing clearly how the volumetric and shear deformation mechanisms contribute in defining the modal characteristics of the embankment. The circular frequency $\omega_{i,n}$ increases as the soil stiffness rises while it reduces with the dimensions of the embankment.

In the case of saturated soil ($V_p >> V_s$) the modal frequencies in the vertical direction are mainly controlled by the volumetric stiffness of water. For the longitudinal motion (Eq. (26)), the effect of the compressional waves is more limited because $\omega_{y,n}$ is inversely proportional to the square of the participating length of the embankment, that is typically much greater than its height (see Section 3.2). It is worth bearing in mind, however, that embankments are generally made of partially saturated, compacted soils in which the compressional velocity is controlled by the stiffness of the soil skeleton. Consequently, the compressional wave velocity of soil V_p is of the same order of magnitude of V_s and the effect of shear deformation on the modal characteristics is significant in the vertical direction as well.

3. Application to a case study

3.1. Reference numerical model

The analytical solutions were tested against the results of a numerical study on the dominant responses of the finite element soil-abutment system depicted in Fig. 3, which is part of the global soil-bridge model developed by Gorini and Callisto (2020) and Gorini (2019) [14,30]. The model was implemented in the analysis framework OpenSees (McKenna 1997, McKenna et al., 2000 [31,32]), while the mesh generation was performed using the pre/postprocessor software GID (Diaz & Amat 1999 [33]). The numerical model includes the abutment, the foundation soil and the approach embankment, comprising a total of 134301 finite elements.

The soil domain was inspired by the case study of the Pantano viaduct (Gorini and Callisto 2017, Gorini 2019 [30,34]), which is the proposed approach structure for the Messina Strait suspension bridge, in Italy (Brancaleoni et al., 2009, Callisto et al., 2013 [35,36]). The foundation soil comprises Messina Gravels (Jamiolkowski and Lo Presti 2002, Fioravante et al., 2012 [37,38]), whose mechanical behaviour was characterised using the Pressure Dependent Multi-Yield model (PDMY) developed by Yang et al. (2003) [39] and calibrated against numerous experimental data relative to monotonic and cyclic conditions. The constitutive parameters assigned to the foundation soil are reported in Table 1, while the reader can refer to Ref. [30] for a detailed description of the calibration procedure. In the model formulation the small strain shear modulus of soil, G_0, increases with the mean effective pressure p' as $G_0 = G_r\,(p'/p_r')^d$, where G_r is the shear modulus relative to a reference effective pressure p_r' and d is a coefficient related to pressure dependency. These parameters were evaluated to reproduce the experimental profile of V_s with depth relative to the Pantano subsoil [30]. The PDMY model is able to reproduce the dependence of the energy dissipation on the strain amplitude. Nonetheless, an additional small

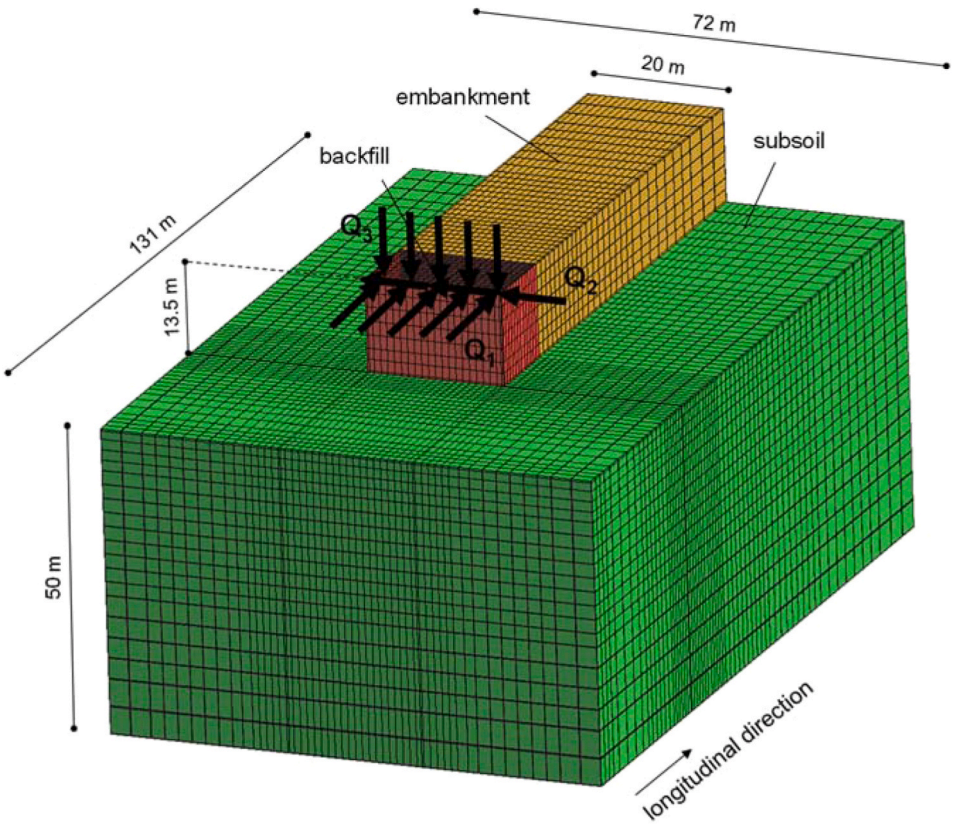

Fig. 3. Mesh of the reference soil-abutment interaction model implemented in OpenSees.

Table 1
Parameters of the PDMY model adopted for the foundation soil and the embankment (Gorini, 2019 [30]).

Variable	Description	Foundation soil	Embankment
ρ (Mg/m^3)	mass density	2.243	2.039
G_r (kPa)	elastic shear modulus at p_r'	1.3×10^5	1.5×10^5
N	Poisson's ratio	0.2	0.2
p_r' (kPa)	reference mean pressure	80.0	80.0
D	pressure dependent coefficient	0.5	0.5
$\gamma_{d,max}$	peak shear strain	0.1	0.1
ϕ_{PTL}	phase transformation angle	26°	26°
C	contraction parameter	0.195	0.195
d_1	dilation parameters	0.6	0.6
d_2		3.0	3.0
M	critical stress ratio	1.54	1.42
λ_c		0.022	0.022
e_0	Critical State Line param.	0.448	0.448
ξ		0.7	0.7
N	number of yield surfaces	40	40

damping ratio equal to 1% was introduced in the soil domain using the Rayleigh formulation in order to attenuate the effects of spurious high frequencies. The subsoil was assumed for simplicity dry and was discretised using the SSPbrick eight-node hexahedral elements (Zienkiewicz and Shiomi 1984 [40]).

Following Gorini (2019) [30], the sandy embankment fill is modelled using an equivalent single-phase body, with the PDMY soil model and input parameters listed in Table 1. To account for the effects of suction (in the partially-saturated fill) the parameters used for the foundation soil were modified considering a different stress ratio at Critical State, a reduced mass density and a modest increment of the elastic moduli.

The soil-structure contact was modelled by means of thin layers meshed by solid elements interposed between the structure and the soil. The behaviour of the interface elements was reproduced through the PDMY model with friction angle equal to that of the soil as a reasonable assumption for rough soil-concrete contact.

The structure presents very similar properties to the abutment of the Pantano viaduct: it is a massive reinforced concrete structure with a 13.5 m-height wall, having a thickness of 4.0 m, resting on a shallow foundation with length and thickness of 17.5 m and 5.0 m, respectively. We assume that the abutment exhibits a linear visco-elastic response, while irreversible displacements occur only in the soil. Hence, all the structural members were modelled through the ShellMITC4 elements (Dvorkin and Bathe 1984 [41]) with elastic behaviour, using constitutive parameters relative to a C32/40 strength class concrete in the European standards EN 206-1. A Rayleigh damping was adopted for the elements of the abutment, calibrated in order to consider a damping ratio not greater than 2% for all the significant modes of the abutment.

After a first calculation stage aimed at reproducing the geostatic stress state, the abutment structure and the embankment were built sequentially in the model. The static analysis was followed by the dynamic simulation, accomplished with parallel computing using the OpenSeesSP interpreter (McKenna and Fenves 2008 [42]) in order to achieve reasonable computation times. The displacements at the bottom of the grid were impeded in both directions, while only the horizontal displacements normal to each boundary were restrained along the lateral sides. The dynamic perturbation consisted of a distributed force of amplitude Q_i (longitudinal Q_1, transverse Q_2 or vertical Q_3) applied to the top of the front wall that varies in time as a harmonic function of period T for 10 cycles of loading, in order to attain a steady-state dynamic response. Different amplitudes were considered with the period ranging between 0.05 and 5.0 s, for a total of 160 analyses carried out for each load direction. In the incremental dynamic analysis, the smallest amplitude of the external force refers to a reversible response of the abutment (i. e. negligible permanent displacements of the abutment top), the latter obtained in the case under examination for $Q_i \leq 1200$ kN/m. The highest external force was instead determined as that perturbation producing a steady dominant response of the abutment, as described in detail later on. The results are expressed in terms of relationships between the external force per unit length of the wall and the corresponding average displacement of the top of the front wall.

3.2. Small strain behaviour

As a first result, let us consider the dynamic identification of the soil-abutment system at small strains ($Q_i \leq 1200$ kN/m). Fig. 4 plots the dynamic amplification curves of the abutment in the three coordinate directions of the deck-abutment contact obtained for $Q_i = 1200$ kN/m, showing the maximum displacements $u_{i,max}$ computed for different periods T of the external perturbation. The figure indicates that a well-defined region of dynamic amplification can be identified for $T = 0.2$–1.0 s (the static response is seen at periods greater than 1.5 s). The peaks of the amplification curves are associated with the vibration modes of the soil-abutment system. Each curve presents a marked monomodal shape, indicating that the dynamic response of the soil-abutment system is essentially controlled by its fundamental mode only, with a dominant period $T_{i,1}$ that depends on the load direction. A stiffer response is obtained in the vertical direction, as indicated by the lowest dominant period $T_{z,1} = 0.4$ s. The transverse response follows quite closely the curve relative to the longitudinal direction but presents a slightly larger dominant period $T_{x,1} = 0.7$ s compared to $T_{y,1} = 0.6$ s for the longitudinal motion. The longer dynamic response in the transverse mode might result from the lack of lateral confinement to the wall: in this direction the vibrations of the abutment are influenced by the interaction with the foundation soil only, causing a slight increment of deformability of the soil-abutment system.

For periods $T > 1.5$ s the dynamic effects become negligible and the external force acts as a static perturbation. The corresponding maximum displacements $u_{i,max}(T > 1.5\text{ s})$ can be therefore used to evaluate the static stiffness of the soil-abutment system, $H_{i,st} = Q_i/u_{i,max}(T > 1.5\text{ s})$. In this case we obtained $H_{x,st} = 4.1$ GN/m, $H_{y,st} = 5.2$ GN/m and $H_{z,st} = 6.4$ GN/m.

The deformations of the abutment are essentially driven by the mass of the large volume of soil (embankment and foundation soil) interacting with the abutment structure, and only to a minor extent by the abutment mass m_{abut}. The relative contribution of these two effects can be inferred looking at Fig. 5 in which the maximum displacement at the top of the abutment $u_{i,max}$, normalised with respect to the displacement u_i,

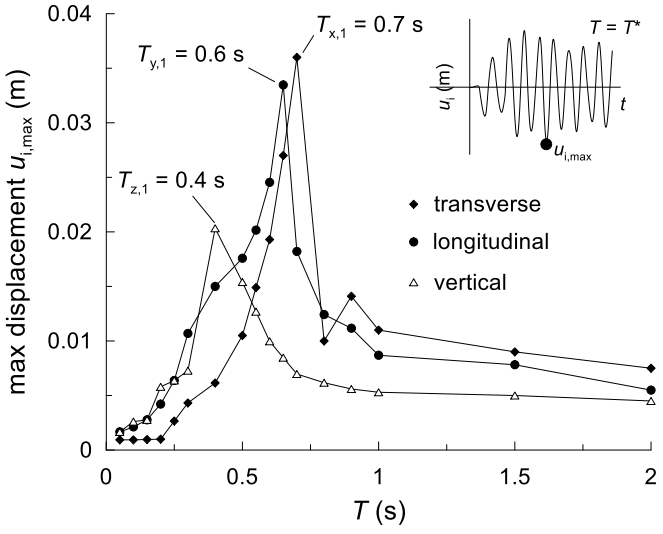

Fig. 4. Dynamic amplification curves of the soil-abutment system in the three translational degrees of freedom of the deck-abutment contact, obtained for an amplitude of the external force $Q_i = 1200$ kN/m (reversible behaviour).

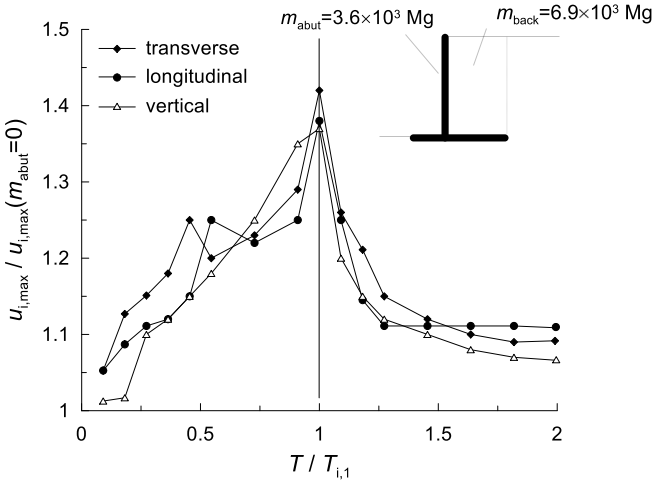

Fig. 5. Effect of the abutment mass m_{abut} on the maximum displacement $u_{i,max}$ of the abutment top in the i-direction plotted as a function of the normalised period $T/T_{i,1}$ ($T_{i,1}$ dominant period of the soil-abutment system in the i-direction).

$_{max}(m_{abut} = 0)$ for an abutment with zero mass, is plotted as a function of the normalised period $T/T_{i,1}$ ($T_{i,1}$ is the dominant period of the abutment with mass in the i-direction). It can be seen that the structural mass produces an increase of the maximum displacement in the region of the maximum dynamic amplification ($0.50 < T/T_{i,1} < 1.25$) but does not affect the dominant period of the soil-abutment system. For all three directions of loading, the maximum ratio $u_{i,max}/u_{i,max}(m_{abut} = 0)$ is equal to about 1.4 occurring at the dominant period of the system. A modal analysis of the abutment structure also shows that its fundamental period, $T_0^{(abut)} = 0.1$ s, is completely decoupled from the dynamic response of the whole system. Hence, it seems reasonable to regard the abutment structure as a rigid body and assume that the dynamic response of the system depends essentially on the mechanical properties of the surrounding soil.

In order to define a calibration procedure for the input parameters of the proposed analytical solutions, the numerical results obtained above are now compared with the dominant periods evaluated through Eqs. (25)–(27). In applying these solutions, the elastic stiffness parameters of the soil listed in Table 1 were used. Since the PDMY model provides a pressure-dependent variation of G_0 with depth (Section 3.1), an average value of the small strain shear modulus of the embankment was used. The resulting compressional and shear wave velocities at small strains correspond to $V_p = 407$ m/s and $V_s = 220$ m/s, respectively. The embankment geometry should be representative of the volume of soil interacting dynamically with the abutment structure. In the numerical simulations the abutment undergoes translational and rotational motions involving part of the embankment and also part of the foundation soil. In a simplified manner, the compliance of the foundation soil was taken into account by introducing an effective height $H_{eff} > H$ in the analytical solutions. Calibrating H_{eff} by trial and error, it was found that the effective height of the embankment can be assumed equal to $H_{eff} = H + 1.5L_f = 26.25$ m, where L_f is the length of the abutment foundation. This best-fit value of the effective height is in a good agreement with typical values of the vertical extension of the soil volume interacting with a shallow foundation (i.e., the abutment foundation), taken equal to $1.5L_f$. The length of the embankment involved in the dynamic response of the abutment, termed "effective length" in the following, was assumed equal to $L_{eff} = 5H = 67.5$ m, as proposed by Gorini and Callisto (2020) and Gorini et al. (2020b) [14,15]. The resulting dominant periods are illustrated in Fig. 6. A comparison with Fig. 4 shows that the periods of the first modes in the three different directions match very well the values obtained by the numerical simulations at small displacements. For the higher-order modes, the vibration period decreases rapidly tending to a horizontal asymptote for $n > 8$.

The analytical solutions also provide the modal masses $m_{i,1}$ (Eq. (15)) and stiffnesses $K_{i,1}$ (Eqs. (16)–(18)) of the embankment. The modal characteristics in the three directions of motion are reported in Table 2 for the first vibration mode. It is interesting to observe that the participating masses $m_{i,1}$ are much larger than the sum of the mass of the abutment structure ($m_{abut} = 3.6 \times 10^3$ Mg) and of the soil above the base of the footing ($m_{back} = 6.9 \times 10^3$ Mg), ranging from 2.3 to 2.7 times the sum of these two masses.

3.3. Effect of the plastic response of the soil

The dominant responses evaluated so far refer to an essentially reversible behaviour of the soil-abutment system. In this section, higher amplitudes of the external forces are considered ($Q_i > 1200$ kN/m) in order to investigate how the dominant responses of a bridge abutment are altered by the nonlinear behaviour of soil.

Table 2
Vibration period T, modal stiffnesses $K_{i,1}$ and modal masses $m_{i,1}$ associated with the first mode of the reference soil-abutment system in the i-direction.

Direction	T (s)	$K_{i,1}$ (GN/m)	$m_{i,1}$ (Gg)	$m_{i,1}/m_{abut+back}$
Longitudinal	0.60	3.19	28.68	2.73
Transverse	0.70	2.15	23.93	2.29
Vertical	0.40	5.62	23.91	2.28

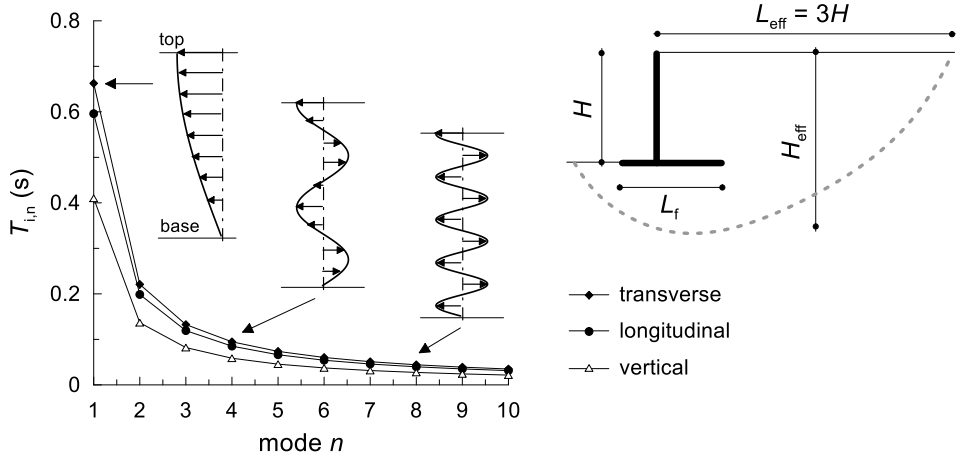

Fig. 6. Analytical evaluation of the vibration periods of the reference embankment in the transverse, longitudinal and vertical directions of motion.

Fig. 7 shows a normalised representation of the dynamic amplification curves of the abutment in the longitudinal direction y, computed for an increasing level of the longitudinal external force Q_1. The normalised maximum displacement $u_{y,max}/u_{y,max}^{(yield)}$ is plotted as a function of the normalised period $T/T_{y,1}^{(yield)}$, where $T_{y,1}^{(yield)} = 0.6$ s is the dominant period at small strains ($Q_1 < 1200$ kN/m) in the longitudinal direction and $u_{y,max}^{(yield)}$ the corresponding maximum displacement. With respect to the small strain response, higher intensities of the external force cause an increment in deformability and a longer dominant response of the abutment. These effects are concisely described by two non-dimensional parameters: the period elongation $T_{y,1}/T_{y,1}^{(yield)}$, where $T_{y,1}$ is the dominant period for a given force Q_1, and the ratio $u_{y,max}/u_{y,max}^{(yield)}$ between the maximum displacements corresponding to Q_1 and $Q_1^{(yield)} = 1200$ kN/m (amplitude that produces the first shift of the dominant period). Fig. 8 summarizes the period elongation and normalised maximum displacements ($T_{y,1}/T_{y,1}^{(yield)}$ and $u_{y,max}/u_{y,max}^{(yield)}$) as functions of the normalised amplitude $Q_1/Q_1^{(yield)}$. These curves highlight some peculiar aspects of the dynamic response of the soil-abutment system. For values of $Q_1/Q_1^{(yield)} < 1$, the maximum normalised displacement $u_{y,max}/u_{y,max}^{(yield)}$ increases quasi-linearly with a modest gradient and the dominant period remains unaltered, characterising a range of the normalised amplitude within which the behaviour of the soil-abutment system is essentially reversible and is governed by the elastic stiffness of the soil. For higher intensities of the external force the behaviour changes, leading to an increment of deformability and a significant increase of the dominant period up to $T_{y,1} = 1.3 \times T_{y,1}^{(yield)} = 0.8$ s. This is a transition region in which the period elongation increases as a consequence of an increasingly more pronounced plastic response of the soil. At higher levels of the external force ($Q_1/Q_1^{(yield)} > 3.0$), the maximum displacements keep increasing more than linearly, but the dominant period stabilises at a value of 0.8 s. This steady dynamic response can be attributed to a diffused plastic response in the soil (ultimate conditions of the soil-abutment system).

The transverse dynamic response of the abutment is summarised in Figs. 9 and 10 and is conceptually similar to that observed in the longitudinal direction. The dynamic amplification curves show a marked mono-modal distribution, with a pronounced maximum value (first mode) and some minor peaks associated with higher-order modes. The dominant period increases progressively from the reversible regime ($T_{x,1}^{(yield)} = 0.7$ s, $Q_2 < 1200$ kN/m) up to a value $T_{x,1}^{(yield)} = 1.0$ s ($T_{x,1}/T_{x,1}^{(yield)} = 1.43$) obtained for an external transverse force $Q_2 > 4800$ kN/m, beyond which the dominant period remains unaltered. Despite the larger dominant period compared to the longitudinal direction, the amplification of the maximum transverse displacements is less pronounced (Fig. 9 vs 7) and this might be associated with the larger size of the foundation in the transverse direction ($B/L_f = 1.6$) that limits the rocking response.

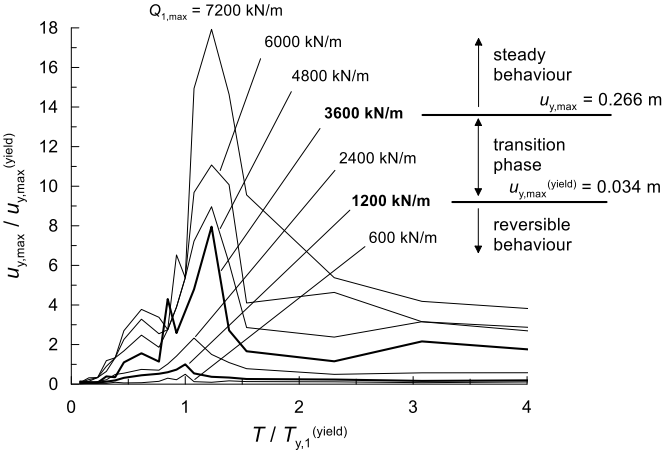

Fig. 7. Normalised dynamic amplification curves of the soil-abutment system in the longitudinal direction, obtained for an increasing amplitude of the external force applied to the abutment top (Q_1 = 600–7200 kN/m).

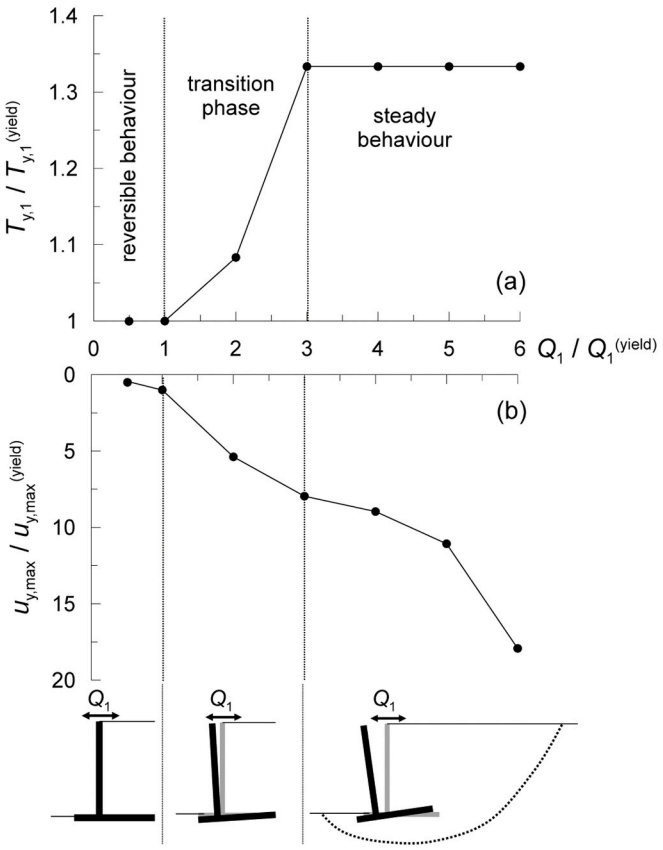

Fig. 8. Normalised curves of (a) the period elongation $T_{y,1}/T_{y,1}^{(yield)}$ and of (b) the maximum displacements $u_{x,max}/u_{x,max}^{(yield)}$ in the longitudinal direction.

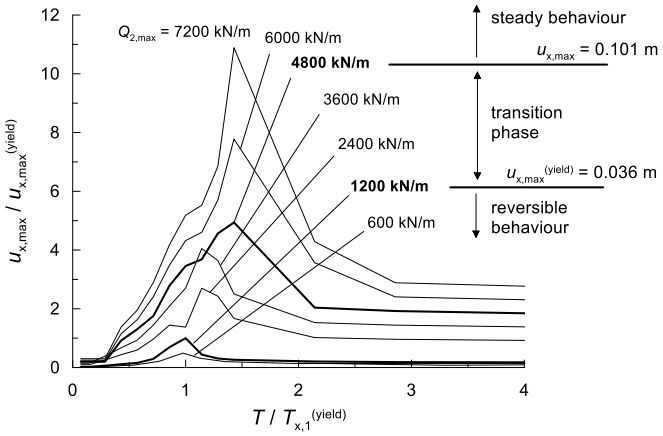

Fig. 9. Normalised dynamic amplification curves of the soil-abutment system in the transverse direction, obtained for an amplitude of the external force Q_2 = 600–7200 kN/m.

In the vertical direction, Figs. 11 and 12, the incremental dynamic analysis consisted in recording the average vertical displacement on the top of the front wall caused by a vertical force Q_3 applied to the same nodes. The reversible behaviour occurs again for $Q_3 < 1200$ kN/m but the vertical response is stiffer ($T_{z,1}^{(yield)} = 0.4$ s) than the horizontal ones. Beyond the reversible regime, the dominant period increases to $T_{z,1} = 0.5$ s at an applied load, $Q_3 = 2400$ kN/m, with a period elongation $T_{z,1}/T_{z,1}^{(yield)} = 1.25$. In this transition phase, the displacements increase markedly. The dominant period does not vary in the range $Q_3 =$

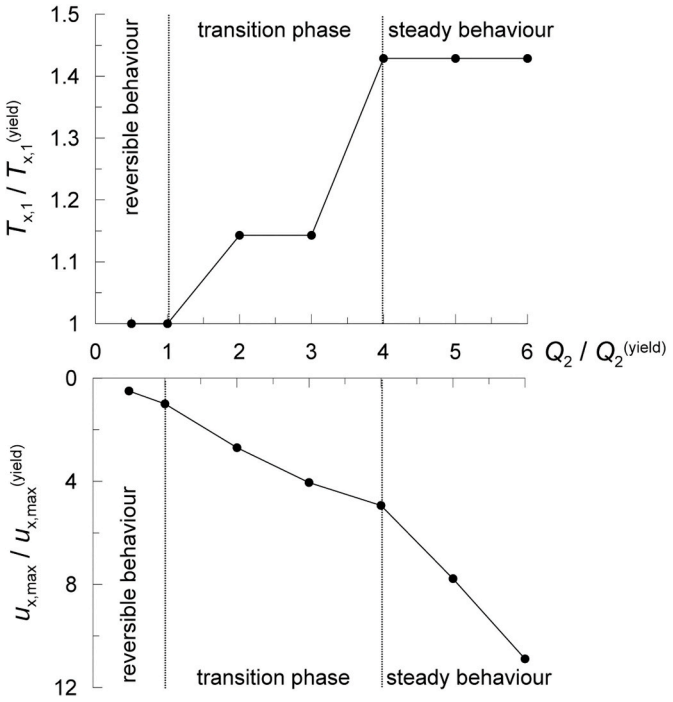

Fig. 10. Normalised curves of (a) the period elongation $T_{x,1}/T_{x,1}^{(yield)}$ and of (b) the maximum displacements $u_{x,max}/u_{x,max}^{(yield)}$ in the transverse direction.

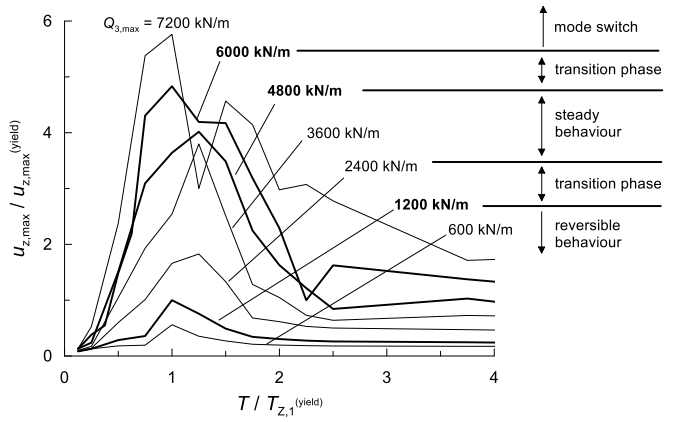

Fig. 11. Normalised dynamic amplification curves of the soil-abutment system in the vertical direction, obtained for an amplitude of the external force Q_3 = 600–7200 kN/m.

2400–4800 kN/m, while the normalised maximum displacements still increase significantly due to the progressively more pronounced plastic response of the soil.

For loads $Q_i \leq 4800$ kN/m, the period elongation is similar for the longitudinal and vertical directions (Figs. 8a and 12a respectively), although the displacement ratio ($u_{z,max}/u_{z,max}^{(yield)}$) is smaller for vertical loading. At higher levels of loading the vertical response exhibits a second transition (Fig. 12) with two dominant periods emerging at Q_3 = 7200 kN/m (T = 0.4, 0.6 s; i.e., $T_{z,1}/T_{z,1}^{(yield)}$ = 1.0, 1.5).

In light of the above, it is evident that the abutment response in the horizontal directions presents a more regular trend of the period elongation where the dominant period increases monotonically from small strains up to a steady dynamic response of the system at large strains. This result can be attributed to the different deformation modes that develop in the soil. A much larger external force is required to activate the global plastic mechanism in the vertical direction, compared to the

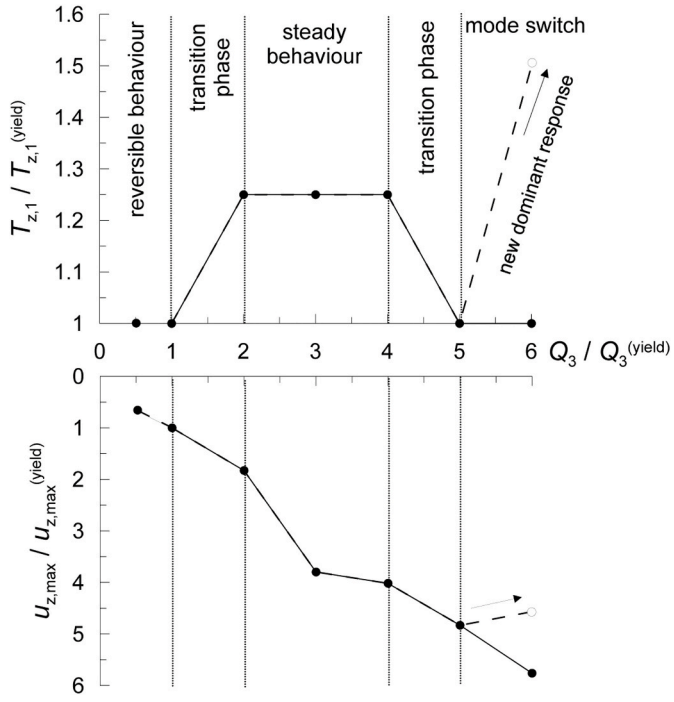

Fig. 12. Normalised curves of (a) the period elongation $T_{z,1}/T_{z,1}^{(yield)}$ and of (b) the maximum displacements $u_{z,max}/u_{z,max}^{(yield)}$ in the vertical direction.

horizontal limit loads [9]. This happens because the bearing capacity of the abutment foundation involves a large volume of soil including zones located in front and behind the abutment wall. This entails a more articulated and progressive mobilization of the soil resistance that might be responsible for the changes in the dominant period observed in Fig. 12.

3.4. Calibration of the analytical solutions for an elastic-plastic response of the embankment

The analytical solutions developed in Section 2 are based on linear soil behaviour, which in principle is acceptable only in the reversible region of the curve of the period elongation. However, the analytical solutions might also provide an adequate representation of the modal characteristics beyond the small strain regime (where there is a progressive reduction in soil stiffness with strain level) using secant equivalent stiffness properties, i.e., by introducing appropriate values of the secant shear modulus degradation ratio, G/G_0. For example, the modulus reduction can be estimated by a free field site response analysis or it can be related to the intensity of the ground motion as reported in Eurocode 8-5 (EN-Eurocode 8-5 Table 4.1).

Regardless of the direction of motion considered, according to Eqs. (25)–(27) the period elongation $T_{i,n}/T_{i,n}^{(yield)}$ rises more than linearly with the modulus reduction, following the logarithmic trend reported below:

$$\frac{T_{i,n}}{T_{i,n}^{(yield)}} = 1 - 0.6 \cdot \ln\left(\frac{G}{G_0}\right), \; i = x, y, z. \tag{28}$$

Fig. 13 shows the optimum values of G/G_0 (obtained by trial and error) to match the dominant periods of the reference abutment with the proposed analytical solutions (Fig. 2) for the longitudinal and vertical directions. It can be seen that the modulus reduction in the transition phase is equal to about 0.9 and 0.8, in the longitudinal and vertical direction respectively, while G/G_0 reaches the values of about 0.55 and 0.65 in the steady state.

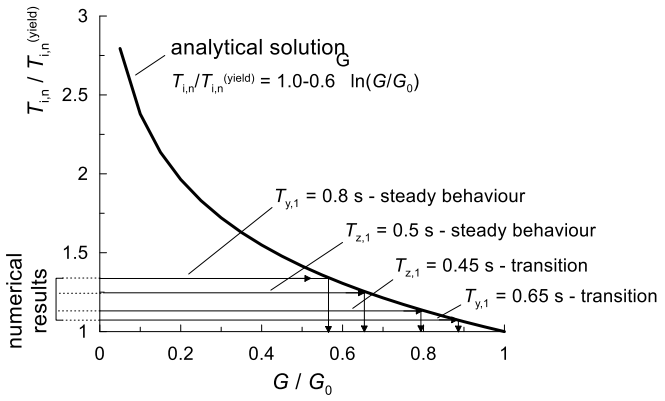

Fig. 13. Analytical evaluation of the dependence of the normalised dominant period $T_{i,1}/T_{i,1}^{(yield)}$ on the normalised shear modulus of the soil G/G_0.

4. Conclusions

In the seismic design of a bridge an important source of uncertainty is the evaluation of the deformability and inertial effects of the bridge abutments, that in turn interact with the approach embankment. This paper contributes to this topic by focusing on the dynamic response of the embankment, evaluated through a closed-form solution, and on its effects on the response of the soil-abutment system, studied with the aid of numerical simulations.

Specifically, the contribution of the embankment can be characterised by its dominant dynamic responses, i.e., by the first vibration modes along the three different directions of motion, and by the corresponding participating masses. These quantities may be found through the analytical expressions obtained in this work, whose calibration requires the shear wave velocity of soil and the evaluation of the significant soil volume interacting with the abutment. For a linear soil behaviour they match quite well the results of a finite-element model of the system, while in the nonlinear regime the same solutions need to consider a secant equivalent soil stiffness, that requires a separate evaluation of an effective strain corresponding to the expected level of mobilised strength in the soil.

A combination of these solutions and the results of the numerical analysis shed some light on the overall dynamic response of the soil-abutment system:

- showing that the inertial effects in the embankment tend to dominate over those associated with the mass of the abutment structure;
- indicating that the vertical dynamic response is somewhat different from that obtained in the horizontal direction;
- indicating the extension of the soil volume that interacts with the abutment for different loading levels;
- illustrating the effects of soil nonlinearity on the dynamic response of the system.

Depending on the design approach used for the bridge, the results of this study may be used in different ways, as follows:

- assist in the selection of dynamic impedances in a spectral analysis of the structure: the proposed identification of the modal masses and stiffnesses of bridge embankments would be aimed to reproduce the frequency-dependent response of the soil-abutment system;
- use the solution to evaluate the small-strain stiffness and the associated mass to include in a plasticity-based macro-element for a time-domain analysis of the bridge.

Declaration of competing interest

The authors declare that they have no known competing financial interests or personal relationships that could have appeared to influence the work reported in this paper.

APPENDIX A

A closed-form expression for the displacement field of the embankment in the longitudinal and vertical directions can be found by solving the equations of motion, Eqs. (7) and (8), by separation of variables. Consider the displacement $u_i(y,z,t)$ decomposed as the product of three mono-variable functions as follows:

$$u_i(y,z,t) = L_i(y) \cdot V_i(z) \cdot T_i(t), \; i = x,y,z. \tag{29}$$

Focusing on the longitudinal motion, substituting Eq. (29) into Eq. (7) and dividing both members of the latter by the total longitudinal displacement $u_y(y,z,t) = L_y(y) \cdot V_y(z) \cdot T_y(t)$, Eq. (7) becomes:

$$\frac{T_{y,tt}(t)}{T_y(t)} - V_p^2 \cdot \frac{L_{y,yy}(y)}{L_y(y)} - V_s^2 \cdot \frac{V_{y,zz}(z)}{V_y(z)} = 0 \tag{30}$$

that is equivalent to the following system of differential equations:

$$\frac{V_{y,zz}(z)}{V_y(z)} = \frac{\mu}{V_s^2} = \mu_z \tag{31}$$

$$a^2 \cdot \frac{T_{y,tt}(t)}{T_y(t)} - \frac{L_{y,yy}(y)}{L_y(y)} = \frac{\mu}{V_p^2} = \mu_y \tag{32}$$

where μ is a coefficient that can be determined from the boundary conditions and $a^2 = V_p^2$.

Eq. (31) admits different solutions depending on the sign of μ_z (an exponential solution if $\mu_z > 0$, a linear solution if $\mu_z = 0$ and a trigonometric solution when $\mu_z < 0$). We consider the case $\mu_z < 0$ since this is the only solution that permits to analyse free vibrations of the embankment; in fact, for $\mu_z = 0$ the system is critically damped and returns quickly without oscillation to equilibrium or steady state, while in the case $\mu_z > 0$ the system is over damped and does not get to oscillate and the transient response of displacement dies pretty slowly. In this case, the generic solution of Eq. (31) reads:

$$V_y(z) = A \cdot \cos\left(z \cdot \sqrt{-\mu_z}\right) + B \cdot \sin\left(z \cdot \sqrt{-\mu_z}\right). \tag{33}$$

The coefficients A and B can be determined by imposing the boundary conditions in the z-direction. Under free vibrations, it is reasonable to assume zero displacements at the base of the embankment ($z = H$) and zero shear strains on top ($z = 0$), namely:

$$V_y(z=H)=0 \tag{34}$$

$$\frac{\partial V_y(z=0)}{\partial z}=0. \tag{35}$$

From Eq. (35) one can obtain $B = 0$ and Eq. (34) gives:

$$u_{y,z}(H)=0 \rightarrow \mu_z=-\frac{\pi^2\cdot(1+2\cdot n)^2}{4\cdot H^2},\ n\in N_0{}^+ \tag{36}$$

by which the coefficient μ can be derived:

$$\mu=\mu_z\cdot V_s{}^2=-V_s{}^2\cdot\frac{\pi^2\cdot(1+2\cdot n)^2}{4\cdot H^2}.\quad n\in N_0{}^+ \tag{37}$$

The expression for the z-dependent function $V_y(z)$ finally reads:

$$V_y(z)=A\cdot\cos\left(z\cdot\sqrt{\frac{\pi^2\cdot(1+2\cdot n)^2}{4\cdot H^2}}\right),\ n\in N_0{}^+. \tag{38}$$

that represents a trigonometric distribution of the longitudinal displacements along the embankment height (N_0^+ indicates the set of natural numbers).

The y-dependent solution $L_y(y)$ is instead computed by means of Eq. (37). The latter can be further decomposed into Eqs. (39) and (40):

$$\frac{L_{y,yy}(y)}{L_y(y)}=\lambda \tag{39}$$

$$\frac{T_{y,tt}(t)}{T_y(t)}=\frac{\lambda+\mu_y}{a^2}=\omega_{y,n}{}^2 \tag{40}$$

The former equation admits a trigonometric solution for $\lambda < 0$:

$$L_y(y)=C\cdot\cos\left(y\cdot\sqrt{-\lambda}\right)+D\cdot\sin\left(y\cdot\sqrt{-\lambda}\right) \tag{41}$$

with C and D integration constants. In the longitudinal direction, it was assumed the conditions of free embankment in correspondence of the abutment wall (no deformations of the soil in contact with the wall) and fixed embankment at an effective distance L from the abutment (see Section 3.2). Accordingly Eq. (41) becomes:

$$L_y(y)=C\cdot\cos\left(y\cdot\sqrt{-\lambda}\right) \tag{42}$$

$$\lambda=-\frac{\pi^2\cdot(1+2\cdot n)^2}{4\cdot L^2},\ n\in N_0{}^+ \tag{43}$$

in which the parameter λ contains the order n of the harmonic (mode) and is inversely proportional to the effective length considered for the embankment (Section 3.2). This implies that the greater the length, the smaller the modal frequency since the deformability of the embankment increases. The coefficient μ_y results to be:

$$\mu_y=\frac{\mu}{V_p{}^2}=-\frac{V_s{}^2}{V_p{}^2}\cdot\frac{\pi^2\cdot(1+2\cdot n)^2}{4\cdot H^2},\ n\in N_0{}^+ \tag{44}$$

and therefore the modal frequencies assume the following form:

$$\omega_{y,n}=\sqrt{\frac{\lambda+\mu_y}{a^2}}=\frac{\pi\cdot(1+2\cdot n)}{2}\cdot\sqrt{\frac{V_p{}^2}{L_{eff}{}^2}+\frac{V_s{}^2}{H_{eff}{}^2}},\ n\in N_0{}^+ \tag{45}$$

that is identical to Eq. (26) obtained through the modal stiffness and mass. As done for the y- and z-dependent functions, the solution of Eq. (40) can be written as:

$$T_y(t)=E\cdot\cos\left(t\cdot\omega_{y,n}\right)+F\cdot\sin\left(t\cdot\omega_{y,n}\right) \tag{46}$$

with E and F determined by imposing the initial conditions $u_y(t = 0) = 0$ and $u_{y,t}(t = 0) = 0$. The overall solution finally yields:

$$u_y(y,z,t) = A \cdot \cos\left(z \cdot \sqrt{-\mu_z}\right) \cdot C \cdot \cos\left(y \cdot \sqrt{-\lambda}\right) \cdot \cdot \left[E \cdot \cos\left(t \cdot \omega_{y,n}\right) + F \cdot \sin\left(t \cdot \omega_{y,n}\right)\right] \cdot \quad (47)$$

The transverse and vertical motion, $u_y(y,z,t)$ and $u_z(y,z,t)$ respectively, can be obtained through Eqs. (6) and (8) by applying again separation of variables as shown above and the general integral is formally identical to Eq. (9).

References

[1] Mackie K, Stojadinovic B. Seismic demands for performance-based design of bridges. Berkeley, CA: University of California; 2003. PEER Report 2003/16. Pacific Earthquake Engineering Research Center.

[2] Kappos AJ, Potikas P, Sextos AG. Seismic assessment of an overpass bridge accounting for non-linear material and soil response and varying boundary conditions. ECCOMAS Themat. Conf. Comput. Methods Struct. Dyn. Earthq. Eng. COMPDYN 2007, Rethymnon, Greece, 2007.

[3] Mitoulis SA. Challenges and opportunities for the application of integral abutment bridges in earthquake-prone areas: a review. Soil Dynam Earthq Eng 2020;135:106–83.

[4] Goel RK, Chopra AK. Seismic response study of the US 101/painter Street overpass using strong motion records. Rep. No. CSM1PI95·01, California Dept. Of Conservation, Div. Of Mines and Geol., Offc. Of strong motion studies, Sacramento. Calif Soil Dynam Earthq Eng 1997;135:106–83.

[5] Werner SD, Beck JL, Levine MB. Seismic response evaluation of Meloland road overpass using 1979 imperial valley earthquake records. Earthq Eng Struct Dynam 1987;15:249–74.

[6] Wilson JC, Tan BS. Bridge abutments: assessing their influence on earthquake response of Meloland road overpass. J Eng Mech 1990;116(8):1838–56.

[7] Shamsabadi A, Ashour M, Norris G. Bridge abutment nonlinear force-deection-capacity prediction for seismic design. J Geotech Geoenviron Eng 2005;1312:151–61.

[8] Shamsabadi A, Rollins KM, Kapuskar M. Nonlinear soil-abutment-bridge structure interaction for seismic performance based design. J Geotech Geoenviron Eng 2007;1336:707–20.

[9] Gorini DN, Whittle AJ, Callisto L. Ultimate limit states of bridge abutments. J Geotech Geoenviron Eng 2020;146(7). https://doi.org/10.1061/(ASCE)GT.1943-5606.0002283.

[10] Kotsoglou K, Pantazopoulou S. Bridge-embankment interaction under transverse ground excitation. Earthq Eng Struct Dynam 2007;36(12):1719–40.

[11] Kotsoglou A, Pantazopoulou S. Assessment and modeling of embankment participation in the seismic response of integral abutment bridges. Bull Earthq Eng 2009;7:343–61.

[12] Elgamal A, Yan L, Yang Z, Conte JP. Three-dimensional seismic response of Humboldt Bay bridge–foundation ground system. J Struct Eng 2008;134(7):1165–76.

[13] Taskari O, Sextos AG. Probabilistic assessment of abutment-embankment stiffness and implications in the predicted performance of short bridges. J Earthq Eng 2015. https://doi.org/10.1080/13632469.2015.1009586. 150218133146008.

[14] Gorini DN, Callisto L. A coupled study of soil-abutment-superstructure interactionvol. 40. Springer Lecture Notes in Civil Engineering "Geotechnical Research for Land Protection and Development" (CNRIG2019); 2020. p. 565–74. https://doi.org/10.1007/978-3-030-21359-6_60.

[15] Gorini DN, Callisto L, Whittle AJ. An inertial macroelement for bridge abutments. Geotechnique; 2020. p. 397. https://doi.org/10.1680/jgeot.19.P.397.

[16] Lam IP, Law H, Kapuskar M. Design for the new san Francisco - Oakland Bay bridge East span, soil-structure interaction problems. Proceedings. Los Angeles: Geo-Institute Conference on Geotechnical Engineering for Transportation Projects, UCLA; July .

[17] Sextos A, Kappos A, Pitilakis K. Inelastic dynamic analysis of RC bridges accounting for spatial variability of ground motion, site effects, and soil-structure interaction phenomena. Part 2: parametric study. Earthq Eng Struct Dynam 2003;32:629–52.

[18] Mylonakis G, Simeonov V, Reinhorn A, Buckle I. Implications of spatial variation of ground motion on the collapse of SR14/I5 southbound separation and overhead in the Northridge earthquake. Seismic response of concrete bridges. Detroit: ACI Spec. Publ. No. SP187, American Concrete Institute; 1999. p. 299–325.

[19] Kramer SL. Geotechnical earthquake engineering. Upper Saddle River, N.J: Prentice- Hall; 1996.

[20] Zhang J, Makris N. Kinematic response functions and dynamic stiffnesses of bridge embankments. Earthq Eng Struct Dynam 2002;31(11):1933–66.

[21] Kotsoglou A, Pantazopoulou S. Response simulation and seismic assessment of highway overcrossings. Earthq Eng Struct Dynam 2009;39:991–1013. https://doi.org/10.1002/eqe.

[22] Mitoulis SA. Seismic design of bridges with the participation of seat-type abutments. Eng Struct 2017;44:222–33.

[23] Stefanidou SP, Sextos AG, Kotsoglou AN, Lesgidis N. Soil-structure interaction effects in analysis of seismic fragility of bridges using an intensity-based ground motion selection procedure. Eng Struct 2017;151:366–80.

[24] Roscoe KH, Schofield AN. The stability of short pier foundations on sand. Br Weld J 1956:343–54.

[25] Nova R, Montrasio L. Settlements of shallow foundations on sand. Geotechnique 1991;41(2):243–56.

[26] Cremer C, Pecker A, Davenne L. Modelling of nonlinear dynamic behaviour of a shallow strip foundation with macro-element. J Earthq Eng 2002;6(2):175–211.

[27] Wilson JC, Tan BS. Bridge abutments: formulation of a simple model for earthquake response analysis. J Eng Mech 1990;116(8):1828–37.

[28] Wissawapaisal C. Modelling the seismic response of short bridges. Champaign (IL): Thesis, University of Illinois at Urbana; 1999.

[29] Clough RW, Penzien J. Dynamics of structures. second ed. Berkeley, California: Computers and Structures; 2003. revised.

[30] Gorini DN. Soil-structure interaction for bridge abutments: two complementary macro-elements. PhD thesis. Rome, Italy: Sapienza University of Rome; 2019.

[31] McKenna F. Object-oriented finite element analysis: Frameworks for analysis, algorithms and parallel computing. PhD thesis. Berkeley, CA: Univ. of California; 1997.

[32] McKenna F, Fenves GL, Scott MH, Jeremic B. Open system for earthquake engineering simulation. 2000. http://opensees.berkeley.edu.

[33] Diaz ND, Amat PS. GID the personal pre/postprocessor user's manual, version 5.0. Barcelona, Spain: CIMNE; 1999. http://gid.cimne.upc.es.

[34] Gorini DN, Callisto L. Study of the dynamic soil-abutment-superstructure interaction for a bridge abutment. Proc. 1st Eur Conf OpenSees (OpenSees Days Europe 2017), Porto 2017:57–60. 978-972-752-221-7.

[35] Brancaleoni F, Diana G, Faccioli E, Fiammenghi G, Firth IPT, Gimsing NJ, Jamiolkowski M, Sluszka P, Solari G, Valensise G, Vullo E. The Messina Strait Bridge. CRC Press; 2009.

[36] Callisto L, Rampello S, Viggiani GMB. Soil-structure interaction for the seismic design of the Messina Strait bridge. Soil Dynam Earthq Eng 2013;52:103–15.

[37] Jamiolkowski M, Lo Presti DCF. Geotechnical characterization of Holocene and Pleistocene Messina sand and gravel deposits. Charact. and Engng. Properties of Natural Soils, vol. 2. Singapore: Balkema Publishers; 2002. p. 1087–11120.

[38] Fioravante V, Giretti D, Jamiolkowski M, Rocchi GF. Triaxial tests on undisturbed samples of gravelly soils from the Sicilian shore of Messina strait. Bull Earthq Eng 2012;10:1717–44.

[39] Yang Z, Elgamal A, Parra E. A computational model for liquefaction and associated shear deformation. J Geotech Geoenviron Eng 2003;129(12):1119–27.

[40] Zienkiewicz OC, Shiomi T. Dynamic behavior of saturated porous media: the generalized Biot formulation and its numerical solution. Int J Numer Anal Methods GeoMech 1984;8:71–96.

[41] Dvorkin EN, Bathe KJ. A continuum mechanics based four node shell element for general nonlinear analysis. Eng Comput 1984;1:77–88.

[42] McKenna F, Fenves GL. Using the OpenSees interpreter on Parallel Computers. 2008. http://opensees.berkeley.edu/OpenSees/parallel/TNParallelProcessing.pdf.